

Image Quality in High-resolution and High-cadence Solar Imaging

C. Denker¹  · E. Dineva^{1,2}  · H. Balthasar¹  ·
M. Verma¹  · C. Kuckein¹  · A. Diercke^{1,2}  ·
S.J. González Manrique^{3,1,2} 

Version: 22 August 2024
© Springer Science+Business Media Dordrecht 2016

Abstract Broad-band imaging and even imaging with a moderate bandpass (about 1 nm) provides a “photon-rich” environment, where frame selection (“lucky imaging”) becomes a helpful tool in image restoration allowing us to perform a cost-benefit analysis on how to design observing sequences for high-spatial resolution imaging in combination with real-time correction provided by an adaptive optics (AO) system. This study presents high-cadence (160 Hz) G-band and blue continuum image sequences obtained with the *High-resolution Fast Imager* (HiFI) at the 1.5-meter *GREGOR* solar telescope, where the speckle masking technique is used to restore images with nearly diffraction-limited resolution. HiFI employs two synchronized large-format and high-cadence sCMOS detectors. The Median Filter Gradient Similarity (MFGS) image quality metric is applied, among others, to AO-corrected image sequences of a pore and a small sunspot observed on 2017 June 4 and 5. A small region-of-interest, which was selected for fast imaging performance, covered these contrast-rich features and their neighborhood, which were part of active region NOAA 12661. Modifications of the MFGS algorithm uncover the field- and structure-dependency of this image quality metric. However, MFGS still remains a good choice for determining image quality without *a priori* knowledge, which is an important characteristic when classifying the huge number of high-resolution images contained in data archives. In addition, this investigation demonstrates that a fast cadence and millisecond exposure times are still insufficient to reach the coherence time of daytime seeing. Nonetheless, the analysis shows that data acquisition rates exceeding 50 Hz are required to capture a substan-

✉ C. Denker
cdenker@aip.de

- ¹ Leibniz-Institut für Astrophysik Potsdam (AIP), An der Sternwarte 16, 14482 Potsdam, Germany
- ² Universität Potsdam, Institut für Physik und Astronomie, Karl-Liebknecht-Straße 24/25, 14476 Potsdam, Germany
- ³ Astronomical Institute of the Slovak Academy of Sciences, 05960, Tatranská Lomnica, Slovak Republic

tial fraction of the best seeing moments, significantly boosting the performance of *post-facto* image restoration.

Keywords: Granulation · Sunspots · Instrumental Effects · Instrumentation and Data Management

1. Introduction

Overcoming the deleterious effects of Earth’s turbulent atmosphere still poses a challenge in ground-based nighttime astronomy and solar observations. The problem of obtaining high-resolution images has been tackled using different approaches, *e.g.* extended surveys to select the best observatory sites, real-time wavefront correction with AO, frame selection or lucky imaging, and advanced image restoration techniques.

The 1.5-meter *GREGOR* telescope (von der Lühé *et al.*, 2001; Volkmer *et al.*, 2010; Denker *et al.*, 2012; Kneer, 2012; Schmidt *et al.*, 2012) is located at Observatorio del Teide, Izaña, Tenerife, Spain. In the late 1960s, the Joint Organization for Solar Observations (JOSO) began a solar site survey, which initially included 40 candidate sites. In 1979, a more thorough survey was carried out on La Palma and Tenerife identifying mountain locations with excellent seeing characteristics (Brandt and Wöhl, 1982). The evaluation of both sites was based on rms-contrast of granulation, image sharpness, image motion, power spectra to derive the Fried-parameter r_0 (Fried, 1965; Fried and Mevers, 1974), and clear daytime fraction per year (about 3000 hours). The results of the JOSO site survey eventually led to the construction of the German solar telescopes on Tenerife (Schröter, Soltau, and Wiehr, 1985; von der Lühé, 1998). Recently, Sprung *et al.* (2016) presented a comprehensive study of the temporal evolution and the local seeing conditions at the *GREGOR* site.

Correlation trackers (von der Lühé *et al.*, 1989; Schmidt and Kentischer, 1995; Ballesteros *et al.*, 1996) were the first attempts to remove rigid image motion and to stabilize time-series data in real-time. They were soon surpassed by AO systems (Acton and Smithson, 1992; Rimmele, 2000) providing instantaneous high-order wavefront correction. Today, all major ground-based solar telescopes are equipped with AO systems, *e.g.* the *Dunn Solar Telescope* in New Mexico (Rimmele *et al.*, 2003), the *Swedish Solar Telescope* at La Palma (Scharmer *et al.*, 2003), the *Goode Solar Telescope* at Big Bear Solar Observatory (*e.g.* Rimmele *et al.*, 2004; Denker *et al.*, 2007a), the *New Vacuum Solar Telescope* at Fuxian Solar Observatory (Rao *et al.*, 2016), and at Tenerife the *GREGOR* solar telescope (Berkefeld *et al.*, 2012) and the *Vacuum Tower Telescope* (von der Lühé *et al.*, 2003). Even for the balloon-borne *Sunrise* telescope, well above the seeing-prone atmosphere, a low-order AO system provided image stabilization and wavefront correction (Berkefeld *et al.*, 2010).

In parallel to the invention of correlation trackers, frame selection was introduced to solar observations (Scharmer, 1989; Scharmer and Löfdahl, 1991; Kitai *et al.*, 1997), which exploits the fact that for short exposure times (a few milliseconds) the wavefront aberrations are constant. Therefore, “freezing” the seeing and picking the best images in a time interval, which is short compared to the evolution time-scale of solar features (a few seconds to a minute at most), yields high-quality time-series. The first implementations of frame selection systems were based on 8-bit video technology and

frame grabbers achieving data acquisition rates of 20–60 Hz. Grabbing images was triggered either by external seeing monitors or by using the high-pass-filtered analog video signal itself. The next improvements concerned synchronized cameras and saving larger sets of images for *post-facto* image restoration. In addition, minimizing the gap between successive exposures (*i.e.* minimizing the seeing-induced polarimetric cross-talk) and the possibility to store larger image sets led to digital magnetograph systems capable of obtaining magnetograms with sub-arcsecond resolution (Lundstedt *et al.*, 1991; Wang *et al.*, 1998). The transition to CCD camera systems with large digitization depths and improved noise characteristics was slow and had the largest impact in nighttime astronomy, where lucky imaging and simple shift-and-add techniques (Law, Mackay, and Baldwin, 2006; Law *et al.*, 2009; Mackay, 2013) significantly enhanced the imaging power of large-aperture telescopes, especially in the visible wavelength regime. Nowadays, the progress in large-format and high-cadence sCMOS detectors (*e.g.* Qiu *et al.*, 2013; Steele *et al.*, 2016, for lucky imaging) offers relatively low-cost detector systems combining the best traits of video and CCD camera systems.

Consequently, the availability of new high-cadence imaging systems and advances in quantifying image quality and in turn seeing conditions, *e.g.* with the MFGS method (Deng *et al.*, 2015), motivated this study. The goals are i) to compare different MFGS implementations, ii) to evaluate potential performance gains in image restoration, when increasing the image acquisition rate, iii) to perform a cost-benefit analysis on how to design observing sequences for high-spatial resolution imaging, iv) to explore the corresponding parameter space and raise awareness for the impacts (benefits and drawbacks) of frame selection in image restoration, and v) to assess ramifications for the next generation of large-aperture solar telescopes and for archives of high-resolution, ground-based solar imaging data.

2. Observations

The observations were taken on 2017 June 4 and 5 with HiFI (Denker *et al.*, 2018b) at the *GREGOR* solar telescope. The targets were a pore and a small sunspot in the leading and trailing parts of active region NOAA 12661, respectively. The continuum images and line-of-sight magnetograms in Figure 1, which were obtained with the *Helioseismic and Magnetic Imager* (HMI, Scherrer *et al.*, 2012) on board the *Solar Dynamics Observatory* (SDO, Pesnell, Thompson, and Chamberlin, 2012), provide a general overview of the active region and precise pointing information. Real-time image correction was provided with the *GREGOR Adaptive Optics System* (GAOS, Berkefeld *et al.*, 2012). The data reduction employed the sTools data processing pipeline (Kuckein *et al.*, 2017), which was developed by AIP's Optical Solar Physics group for high-resolution solar imaging and imaging spectropolarimetry (Denker *et al.*, 2018a). The sTools source code and HiFI data are available at AIP's *GREGOR* archive webpages (GREGOR.aip.de) after user registration.

Average dark and flat-field frames were applied to the HiFI data. A large number of flat-field frames ($n = 2000$) were taken close to the center of the solar disk while the telescope pointing followed a circular path, thus, smearing out the granular pattern and on average providing a uniform illumination of the detector. Sensitivity and noise

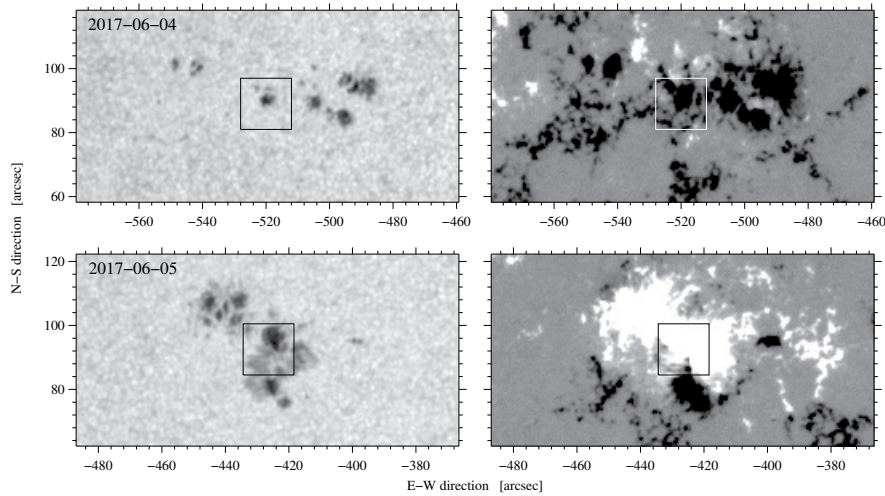


Figure 1. Continuum images (*left*) and line-of-sight magnetograms (*right*) of active region NOAA 12661 observed with HMI at 08:00 UT on 2017 June 4 (*top*) and at 09:00 UT on 2017 June 5 (*bottom*). The axes refer to disk center coordinates. The selected ROI for HiFI observations is highlighted by square boxes.

characteristics of sCMOS detectors differ from CCD technology because of active pixels, which can be considered as small read-out circuits. Therefore, these properties are unique for each pixel and can vary significantly across the detector (*e.g.* Qiu *et al.*, 2013).

The two HiFI cameras are synchronized by a programmable timing unit (PTU) with microsecond precision. The exposure time for both detectors was either $t_{\text{exp}} = 1.2$ or 1.5 ms depending on the elevation of the Sun and the sky brightness. Two interference filters with a full-width-at-half-maximum (FWHM) of about 1.1 nm selected two spectral windows, *i.e.* the Fraunhofer G-band $\lambda 430.7$ nm and a blue continuum window $\lambda 450.6$ nm, where in the latter spectral lines are sparser than in the neighboring parts of the solar spectrum. Different count rates in both imaging channels were adjusted by inserting suitable combinations of neutral density filters in the brighter channel. The field-of-view (FOV) of both cameras was carefully aligned by inserting pinholes and a resolution target in the focal plane F3 of the *GREGOR* telescope (see Soltau *et al.*, 2012). Thus, both cameras record the same scene on the Sun at the same time under exactly the same seeing conditions. The light path is the same for both imaging channels with the exception of the final beamsplitter cube separating the two imaging channels. Thus, optical aberrations are virtually the same in both channels because aberrations introduced by the final beamsplitter cube are negligible.

The Imager sCMOS cameras from LaVision in Göttingen have 2560×2160 pixels but for this application only a region-of-interest (ROI) of 640×640 pixels was selected, increasing the data acquisition rate from about 50 to 160 Hz. The dynamic range of the images is 16 bits. Thus, the sustained writing speed to a RAID-0 array of eight 500-GB solid-state-drives (SSDs) is 250 MB s^{-1} . An imaging sequence consisted typically of 50 000 or 100 000 images in each channel. However, the fast acquisition rates caused intermittent synchronization errors between image acquisition and writing, so that the

actually recorded number of frames is lower. Consequently, short interruptions occurred when the cameras were restarted. The observing characteristics are summarized in Table 1, which is based on $n_4 = 451\,347$ and $n_5 = 243\,871$ image pairs for 2017 June 4 and 5, respectively. The total data volume is 1.1 TB including calibration frames. The comprehensive analysis of the HiFI data required several CPU weeks on regular desktop computers and multi-core compute servers for the image restoration. However, neither real-time processing nor real-time frame-selection is the primary goal of this study but can be accomplished for some of the image quality metrics by streamlining the implementation of the algorithms, by binning the data before calculating the metrics, by selecting smaller ROIs for the computation of the metrics, and by using multi-core or specialized graphical processing units (GPUs). In general, MFGS is not very computationally efficient considering the convolution with gradient operators and the median filter as a special kind of order-statistics filter. Some more basic but robust and efficient approaches for real-time frame selection were already mentioned in Section 1.

3. Results

Both datasets on 2017 June 4 and 5 are included in the analysis because on the first day the scene on the Sun comprised a relatively simple pore and some granulation. This allows us to compute the granular rms-contrast c_{rms} , which is typically used to evaluate image quality and seeing conditions. However, the seeing conditions were better on June 5 with the Fried-parameter r_0 reaching up to 15 cm as compared to a maximum value of $r_0 = 10$ cm on June 4. Thus, the seeing conditions were either very good or good on these two observing days but not excellent. Some of the best images from the *GREGOR* solar telescope were presented by Schlichenmaier *et al.* (2016). The scene on the second day comprised the central part of a small sunspot with umbral dots and strongly twisted penumbral filaments. The r_0 -values are typically derived from the variance of the total mode wavefront error measured by GAOS, which records it and saves it into the state database of the *GREGOR* Telescope Control System (TCS, Halbgewachs *et al.*, 2012) along with other telescope information. Unfortunately, this recording mechanism was not available for GAOS data during the observations in June 2017 because of an erroneously set debugging flag in the control software so that only the maximum r_0 -values from the GAOS user interface were at hand as written down in the observing notes.

3.1. Median Filter Gradient Similarity

The MFGS image quality metric was introduced to solar physics by Deng *et al.* (2015) to evaluate high-spatial resolution images. First, a two-dimensional median filter F with a size of 3×3 pixels is applied to the raw image A , which yields an image $B = F(A)$ with diminished noise. In a second step, the magnitude gradients $G_A = G(A)$ and $G_B = G(B)$ are computed for both the raw and the filtered image. In the original implementation, the gradient magnitude is replaced by just a directional derivative $G = |G_x|$, for example, in the x -direction, to speed up the processing time. However, the magnitude gradient operator

$$G = \sqrt{G_x^2 + G_y^2} \quad (1)$$

can be implemented more fittingly as a convolution of the images A and B using the Scharr (2007) derivative operators

$$G_x = \frac{1}{16} \begin{bmatrix} -3 & 0 & 3 \\ -10 & 0 & 10 \\ -3 & 0 & 3 \end{bmatrix} \quad \text{and} \quad G_y = \frac{1}{16} \begin{bmatrix} 3 & 10 & 3 \\ 0 & 0 & 0 \\ -3 & -10 & -3 \end{bmatrix}, \quad (2)$$

which contain some desirable smoothing abilities and remove much of the directional preference when taking just derivatives. The Scharr gradient operator resembles the Sobel and Prewitt edge enhancement operators but contains different matrix elements. The normalization factors for G_x and G_y can be omitted because they cancel when calculating the MFGS. The borders of the images have to be treated appropriately in both the median filter and convolution.

Finally, following Deng *et al.* (2015), the MFGS value is computed as

$$m, m' = \frac{2(\sum G_A)(\sum G_B)}{(\sum G_A)^2 + (\sum G_B)^2}, \quad (3)$$

where the symbol $\sum \dots$ indicates the sum over all pixels in the gradient images. The variables m and m' stand for the directional derivative $G = |G_x|$ and the magnitude gradient based on the Scharr operators (Equation 1), respectively. In addition, the MFGS algorithm was slightly altered when determining the MFGS locally, on a pixel-by-pixel basis before taking the sum, again using the magnitude gradient based on the Scharr operators

$$m^* = \sum \left(\frac{2G_A G_B}{G_A^2 + G_B^2} \right), \quad (4)$$

where the fraction within the parenthesis refers to a two-dimensional MFGS map. While the MFGS value for a single pixel is certainly not a meaningful descriptor of image quality, contributions to the MFGS metrics of dissimilar features in the FOV become more easily apparent. Taking averages over statistically meaningful samples, which do not have to be contiguous, can then be related to image quality. All image quality metrics fulfill the condition $m, m', \text{ and } m^* \in (0, 1]$. The upper limit $m = 1$ is only reached, if both magnitude gradients are identical $G_A = G_B$. In the local case, m^* is undefined for a very limited number of pixels, where all values within a 3×3 -pixel neighborhood are identical. These pixels have to be appropriately replaced in the two-dimensional maps and discarded before taking the averages.

3.2. Temporal Evolution of Seeing Conditions

The temporal evolution of the image quality is summarized in the top and middle panels of Figure 2 for the high-cadence blue continuum and G-band time-series. Computing the original MFGS value m for each image yields profiles closely related to the prevailing seeing conditions. The image quality metric m is highly correlated for both imaging channels and exhibits slightly higher values for the G-band observations. In principle, MFGS values are wavelength dependent and influenced by the morphological contents of an image. The former dependency results in larger MFGS values for longer

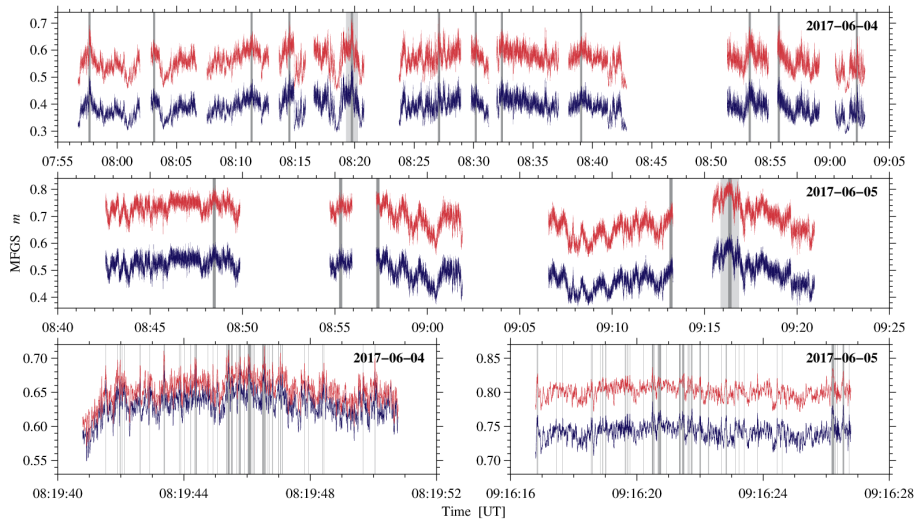


Figure 2. Temporal evolution of the original MFSG value m on 2017 June 4 (*top*) and 2017 June 5 (*middle*). The moments of best seeing are marked by thin, dark gray rectangles indicating a 10-second interval. The very best moments on each day are surrounded by broader rectangles in lighter gray indicating a 1-minute time interval. The MFSG records for the blue continuum images (*blue*) are displaced by 0.15 downwards to separate them from the G-band values (*red*) to facilitate better comparison. The MFSG values are displayed in two panels (*bottom*) at higher temporal resolution for the best 10-second intervals on both observing days. No offsets are applied. The very best $n_{\text{sel}} = 100$ images, which are selected as input for speckle masking image restoration, are marked by gray vertical lines.

wavelength as the seeing improves with increasing wavelength. However, the wavelength difference between the blue continuum window and the G-band spectral range is only 20 nm and thus negligible. The latter dependency is more relevant in this context because G-band images contain high-contrast bright-points caused by small-scale flux concentrations. These peculiarities of magnetized radiative transfer are exploited in proxy-magnetometry (Steiner, Hauschildt, and Bruls, 2001; Leenaarts *et al.*, 2006).

A total of 12 and 5 image sequences of varying length were recorded on June 4 and 5, respectively, resulting in a 66- and a 37-minute time-series. The cause of the interruptions was already mentioned in Section 2. The mean MFSG values m , m' , and m^* are given in Table 1 along with the rms-contrast c_{rms} , which refers to a small region with granulation on June 4 but covers the entire ROI on June 5. Therefore, the contrast values are not directly comparable on both days. The implementation of the MFSG methods significantly affects the statistical properties and moments of m , m' , and m^* , as is evident for the mean values of the image sequences. The following Section 3.3 provides a more detailed correlation analysis of the various image quality metrics. On June 5, the original MFSG value m is on average $\Delta m = 0.12$ and 0.14 higher than on the previous day for the blue continuum and G-band images, respectively. In general, the separation between the original MFSG values m for blue continuum and G-band images increases with better seeing. The MFSG time-profiles exhibit substantial variations on all time-scales, *i.e.* across the image sequences, the time-series, and the observing days. Therefore, the MFSG time-profiles in Figure 2 impressively demonstrate the potential for frame selection in high-resolution solar imaging and illustrates the expected performance gains.

Table 1. Observing characteristics and image quality parameters on 2017 June 4 and 5.

No.	Date	Start	t_{exp}	n_{seq}	Blue continuum					G-band				
					m	m'	m^*	c_{rms}	m	m'	m^*	c_{rms}		
1	2017-06-04	07:56:42 UT	1.5 ms	50 000	0.521	0.855	0.745	1.95%	0.541	0.874	0.759	2.87%		
2	2017-06-04	08:02:51 UT	1.5 ms	36 702	0.529	0.865	0.753	2.06%	0.550	0.884	0.767	3.09%		
3	2017-06-04	08:07:33 UT	1.5 ms	50 000	0.542	0.877	0.761	2.25%	0.569	0.898	0.778	3.75%		
4	2017-06-04	08:13:37 UT	1.5 ms	21 554	0.542	0.873	0.761	2.58%	0.564	0.890	0.774	3.65%		
5	2017-06-04	08:16:34 UT	1.5 ms	40 514	0.549	0.878	0.764	2.65%	0.567	0.891	0.774	3.43%		
6	2017-06-04	08:23:43 UT	1.2 ms	50 000	0.546	0.879	0.763	2.31%	0.572	0.898	0.776	3.00%		
7	2017-06-04	08:29:47 UT	1.2 ms	14 321	0.544	0.877	0.761	2.17%	0.570	0.895	0.773	2.87%		
8	2017-06-04	08:31:56 UT	1.2 ms	50 000	0.553	0.886	0.769	2.32%	0.580	0.905	0.783	3.66%		
9	2017-06-04	08:37:59 UT	1.2 ms	46 940	0.533	0.865	0.753	2.30%	0.558	0.886	0.767	3.62%		
10	2017-06-04	08:51:21 UT	1.2 ms	33 344	0.545	0.879	0.764	2.50%	0.571	0.898	0.777	3.45%		
11	2017-06-04	08:55:34 UT	1.2 ms	33 918	0.529	0.864	0.752	2.16%	0.552	0.885	0.767	3.20%		
12	2017-06-04	09:00:26 UT	1.2 ms	24 054	0.500	0.829	0.729	1.90%	0.515	0.847	0.740	2.88%		
				451 347	0.537	0.870	0.757	2.26%	0.560	0.889	0.770	3.32%		
1	2017-06-05	08:42:35 UT	1.2 ms	69 911	0.676	0.959	0.840	16.05%	0.733	0.973	0.859	18.20%		
2	2017-06-05	08:54:44 UT	1.2 ms	11 644	0.672	0.957	0.837	15.61%	0.728	0.971	0.856	17.74%		
3	2017-06-05	08:57:14 UT	1.2 ms	44 689	0.639	0.943	0.822	12.61%	0.691	0.961	0.842	14.53%		
4	2017-06-05	09:06:33 UT	1.2 ms	64 612	0.603	0.926	0.804	10.27%	0.649	0.946	0.824	11.99%		
5	2017-06-05	09:15:25 UT	1.2 ms	53 015	0.653	0.948	0.828	13.08%	0.709	0.964	0.848	15.08%		
				243 871	0.644	0.945	0.824	13.22%	0.698	0.961	0.844	15.18%		

The two panels in the bottom row of Figure 2 display 10-second MFGS time-profiles during the moments of best seeing (taken from image sequences No. 5 on both observing days). These moments are also marked by thin, dark gray rectangles in the top and middle panels for each image sequence. The very best moments are highlighted by broader rectangles in light gray corresponding to a 1-minute time interval. Out of the $n_{\text{set}} = 1600$ images per 10-second time interval only $n_{\text{sel}} = 100$ images are selected for subsequent image restoration. These instants are indicated by gray vertical lines, which cover the entire 10-second time interval. However, both MFGS time-profiles on June 4 and 5 exhibit a tendency of clustering, *i.e.* some 5–10 high values occur almost consecutively. These clusters of a few high MFGS values can likely be expanded by increasing the data acquisition rate by a factor 5–6 considering the 1-millisecond exposure times, if faster detectors become available. As a result, the time interval can be shortened to acquire images with statistically independent wavefront aberrations required for image restoration. The current data acquisition rate of $f_{\text{acq}} = 160$ Hz is still insufficient to reach the point, where wavefront aberrations are constant in consecutive images. The above frame selection parameters are similar to the current HiFI default observing sequence, which uses $n_{\text{sel}} = 100$ and $n_{\text{set}} = 500$ for a 10-second time interval. The later parameter is lower because full-format frames with 2×5 megapixels are recorded and not just small ROIs. These settings can of course be adapted to a specific science case – as in this study. Since frame selection is performed after image acquisition, it is usually known, if interesting transient events occurred (for example flares). In this case, or if the data were taken under excellent seeing conditions, all images will be kept to retain the highest temporal evolution or to zoom in on a particular time period.

Visually judging and ranking image quality for high-resolution images is a relatively simple task and requires only minimal training (*e.g.* Zirin and Mosher, 1988). However, the huge data volume renders this task impracticable and even impossible for high-cadence and high-resolution solar images. The observations on June 4 and 5 covered a wide range of seeing conditions. Figure 3 relates the visual impression of image quality to the quantitative MFGS value m . This value is given just for the G-band images in equidistant steps of $\Delta m = 0.05$. On both observing days, image sequences No. 5 were used to find G-band images, where the MFGS values closely match the thus defined thresholds ($m = 0.45, 0.50, 0.55, \dots$). The corresponding values for the blue continuum images are on average lower by $\Delta m = 0.02 - 0.05$ but follow the same trend. Below the threshold of $m = 0.5$ for G-band images, solar fine structure like the granulation pattern completely vanishes, and only strong features like dark pores persevere. A MFGS threshold of $m > 0.65$ for G-band images is a good choice for image restoration using the above frame selection criterion (best $n_{\text{sel}} = 100$ images out of $n_{\text{set}} = 1600$ images in a 10-second time interval). However, on June 4, this criterion is only fulfilled for $N_{\text{set}} = 9$ out of 277 possible 10-second intervals. On June 5, the seeing conditions are much improved, so that the criterion is surpassed in $N_{\text{set}} = 143$ out of 150 cases. An even stricter criterion of $m = 0.75$ for G-band images still yields about one third of all possible 10-second intervals.

The following sections illustrate the results of the analysis using subsets (June 4 or 5 as well as G-band or blue continuum images) of the image sequences for reasons of conciseness but the findings are based on the complete dataset. Notwithstanding, major differences are explicitly noted.

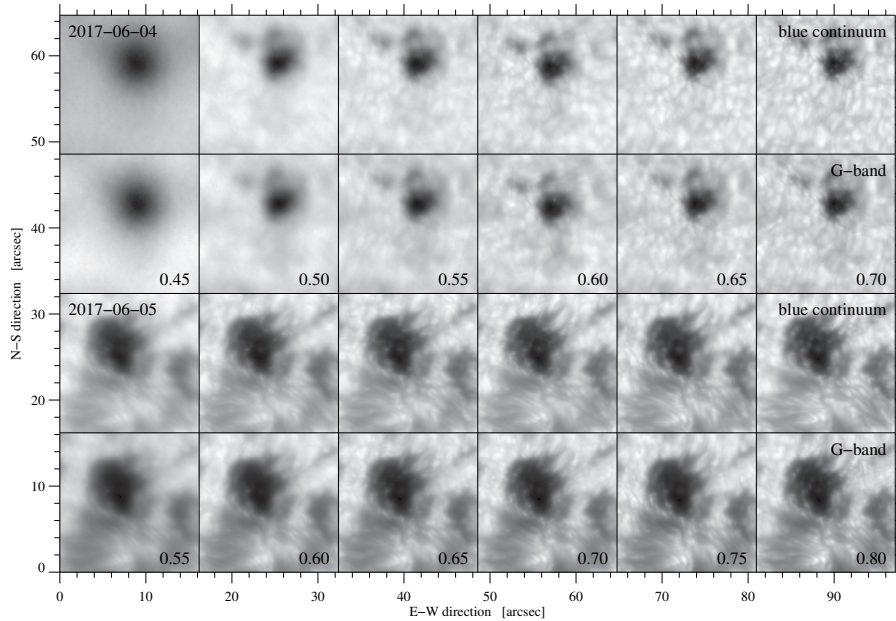


Figure 3. Blue continuum and G-band images of a pore (*top two rows*) and a small sunspot (*bottom two rows*) in active region NOAA 12661 observed with HiFI on 2017 June 4 and 5, respectively. The images are normalized with respect to the quiet-Sun intensity I_0 and displayed in the range $I/I_0 \in [0.4, 1.1]$ and $I/I_0 \in [0.5, 1.2]$, respectively. The original MFGS value m is given in the bottom-right corner for the G-band images.

3.3. Correlations between Image Quality Metrics

In this study, four parameters are used to describe image quality and in turn the prevailing seeing conditions, *i.e.* the granular rms-contrast c_{rms} and three implementations of MFGS m , m' , and m^* . The goal of the correlation analysis is to determine relationships among these parameters and to identify differences when comparing blue continuum and G-band images.

The granular rms-contrast c_{rms} is commonly used to characterize seeing conditions relying on the uniform and isotropic properties of granulation. However, granulation exhibits a distinct center-to-limb variation (*e.g.* Wilken *et al.*, 1997; Carlsson *et al.*, 2004), experiences geometric foreshortening close to the solar limb, and depends on the observed wavelength (*e.g.* Wedemeyer-Böhm and Rouppe van der Voort, 2009). In addition, telescope optics and instrumental straylight have a significant impact on the granular contrast. Only the images observed on June 4 contain a considerable fraction of granulation. Thus, the correlation analysis is based on these data. Computing MFGS values for the region with granulation or the entire FOV only results in minor differences, thus MFGS values are based on the full FOV. Note that the rms-contrast for the sunspot with rudimentary penumbra is an order of magnitude higher than that of granulation, which motivates the search for image quality metrics with weak or negligible dependency on the observed scene on the solar surface.

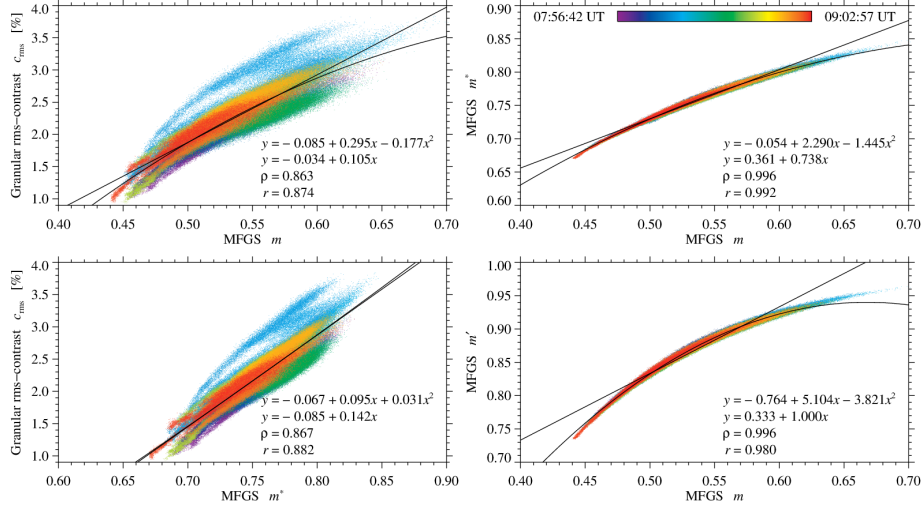


Figure 4. Scatter plots of granular rms-contrast c_{rms} and various MFGS implementations m , m' , and m^* for the 2017 June 4 G-band images. The observing time is color coded according to the scale bar in the top-right panel. However, some of the earlier data points are covered by those obtained later. The black lines and curves represent linear and parabolic models, respectively, where the corresponding mathematical expressions are given in the bottom-right corner of the panels along with Pearson's linear correlation coefficient r and Spearman's rank-order correlation coefficient ρ .

The two left panels of Figure 4 compare the rms-granular contrast c_{rms} with the two image quality metrics m and m^* for blue continuum images. Both scatter plots show a broad distribution around the linear regression line. Even a 2nd order polynomial does not improve the regression. Visual inspection of the two scatter plots hints at a more linear dependency between c_{rms} and the local MFGS implementation m^* as compared to the original MFGS procedure m by Deng *et al.* (2015). These authors already mentioned that the (granular) rms-contrast has an inferior performance compared to MFGS methods. On the other side, the region with granulation is relatively small containing only a few tens of granules. Therefore, the temporal evolution of granules potentially affects the rms-contrast because the sample is too small violating the assumption that granulation is on average uniform and isotropic.

The two right panels of Figure 4 compare the two alternative MFGS implementations m' and m^* to the original approach for the MFGS metric m by Deng *et al.* (2015). The correlations in these scatter plots are much tighter, though not linear. However, the trend in the scatter plots is monotonically increasing, and a 2nd order polynomial fit already provides satisfactory regression results, capturing the functional dependency. Interestingly, just switching from the directional derivative to the magnitude gradient based on Scharr operators (see Section 3.1) deviates from a linear model and changes the range of MFGS values considerably. Note that the range of values is kept similar for abscissae and ordinates in the panels of Figure 4 facilitating easier visual comparison. The deviation from a linear model is even stronger for the local MFGS values m^* but the monotonic trend in the scatter plot still allows to establish a strict functional dependency between m and m^* . *Ab initio*, this is not anticipated but justifies determining the MFGS

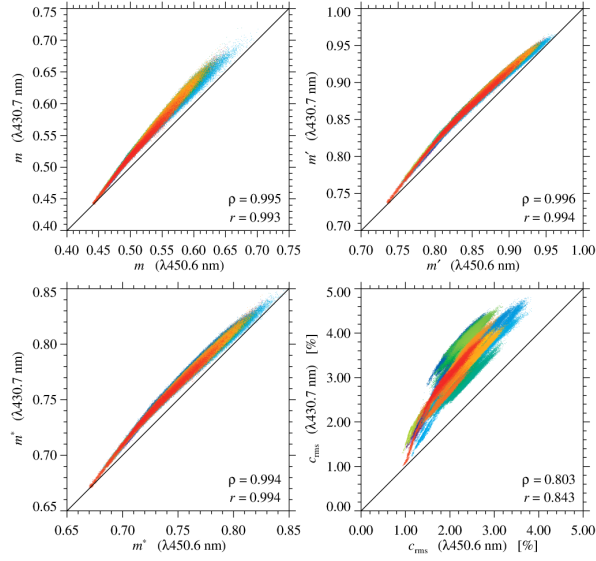


Figure 5. Scatter plots of granular rms-contrast c_{rms} and various MFGS implementations m , m' , and m^* comparing the same parameters for blue continuum and G-band images observed on 2017 June 4. The color code is the same as in Figure 4, and Pearson’s linear correlation coefficient r and Spearman’s rank-order correlation coefficient ρ are given in the bottom-right corner of the panels.

locally, on a pixel-by-pixel basis – thus gaining access to the structure-dependency of MFGS within the observed FOV.

Even though observed at neighboring wavelengths, the morphological differences between blue continuum and G-band images lead to noticeable variations in the four image quality respectively seeing parameters c_{rms} , m , m' , and m^* . The parameters for blue continuum and G-band images do not coincide with the line of equality in the scatter plots of Figure 5. The G-band values are always above the identity line. For m' and m^* , the values approach the identity line only for the lowest and highest values, indicating that either the fine structure is completely washed out in bad seeing conditions or that the seeing is so good that the discriminatory power of both MFGS implementations becomes very similar. The former effect is also observed for c_{rms} and m . However, under good seeing conditions, the trendline becomes more parallel to the line of equality. As in Figure 4, the values of the granular rms-contrast are widely dispersed in the scatter plot shown in the bottom-right panel of Figure 5. These trends are also reflected in Pearson’s linear correlation coefficients r and Spearman’s rank-order correlation coefficients ρ , given in the bottom-left corner of the plot panels, which are much lower for the rms-granular contrast c_{rms} than for the MFGS parameters m , m' , and m^* .

3.4. Impact of Image Acquisition Rate

The high-cadence time-series of blue continuum and G-band images allow us to evaluate the impact of the image acquisition rate f_{acq} on the image quality metrics m after selecting the best images for image restoration. For this numerical experiment,

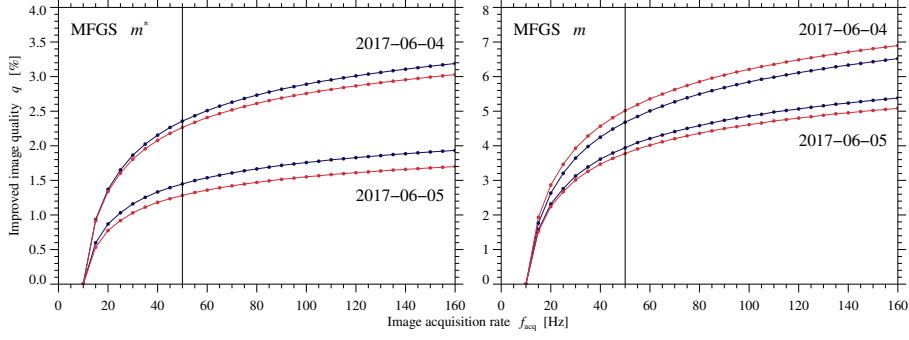


Figure 6. Improvement of the image quality q as a function of the image acquisition rate f_{acq} when using frame selection ($n_{\text{sel}} = 100$ images). The quality parameters $q(f_{\text{acq}})$ are computed based on the local MFGS m^* (left) and on the original implementation of the MFGS m (right), which are given for both observing days and the blue continuum (blue) and G-band (red) images. The bullets mark the image quality measurements at intervals of 10 Hz. The vertical lines at $f_{\text{acq}} = 50$ Hz refer to the data acquisition rate of full-format sCMOS frames.

$n_{\text{sel}} = 100$ images are selected in a time interval $\Delta t_{\text{set}} = 10$ s, which contains a set of $n_{\text{set}} = 1600$ images. Thus, the total number of consecutive sets is $N_{\text{set}} = 427$ on both observing days. The MFGS values $m_{i,j}$ refer to individual images in a set, whereas m_i relates to all MFGS values in a given set, and \bar{m}_i is the mean value of all $n_{\text{set}} = 1600$ images in a set. The improvement in the image quality metrics m is given in percent by the expression

$$q(f_{\text{acq}}) = \frac{100\%}{N_{\text{set}}} \sum_{i=1}^{N_{\text{set}}} \frac{\bar{m}_i(f_{\text{acq}}) - \bar{m}_i}{\bar{m}_i} \quad \text{with} \quad (5)$$

$$\bar{m}_i = \frac{1}{n_{\text{set}}} \sum_{j=1}^{n_{\text{set}}} m_{i,j} \quad \text{with} \quad \bar{m}_i(f_{\text{acq}}) = \frac{1}{n_{\text{sel}}} \sum_{j=1}^{n_{\text{sel}}} \text{best}(n_{\text{acq}}, m_{i,j}), \quad (6)$$

where the function $\text{best}(\dots)$ selects the best $n_{\text{sel}} = 100$ images from a subset of $n_{\text{acq}} = 100, 150, 200, \dots, n_{\text{set}}$ images, which are evenly spaced within a set of n_{set} images. Thus, n_{acq} corresponds to the images acquisition rate f_{acq} . Since $n_{\text{set}} \bmod n_{\text{acq}} \neq 0$ in many cases, the indices of the n_{acq} images were first computed as real numbers before casting them with the floor function to integers.

The results from this numerical experiment are presented in Figure 6 for both observing days, both the blue continuum and G-band images, and both image quality metrics m^* and m . At the data acquisition rate $f_{\text{acq}} = 10$ Hz, the image quality basically remains the same, as no image selection is carried out. Slight differences only arise from the coarser sampling of the time interval $\Delta t_{\text{set}} = 10$ s with $n_{\text{sel}} = 100$ instead of $n_{\text{set}} = 1600$ images. At higher frequencies, the image quality improves monotonically, with most of the gain at frequencies below $f_{\text{acq}} = 50$ Hz, which is, by coincidence, also the data acquisition rate of the HiFi sCMOS sensors when reading out full-format frames. Even though higher frame rates are desirable, off-the-shelf and state-of-the-art sCMOS detectors are already a very good choice for high-resolution solar imaging.

By visual comparison, the improvement of image quality based on the MFGS value m is about twice that of m^* . However, considering that the range covered by both im-

age quality metrics also differs, the absolute improvement in percent is not a decisive factor. The slopes of $q(f_{\text{acq}})$ for higher image acquisition rates, however, indicate that the original MFGS m is more sensitive to changes of the image quality in this region. Typically, the blue continuum images experience a larger improvement of the image quality, with exception of the MFGS values m on June 4. A likely explanation is the directional derivative in the original implementation by Deng *et al.* (2015). Using the gradient magnitude based on Scharr operators but the same summation scheme as in Deng *et al.* (2015) already delivers MFGS values m' very similar to those in the left panel of Figure 6 for the local MFGS m^* . If the seeing conditions are moderately good, as they were on June 4, the marginal benefits of frame selection are higher than on days, when the seeing is very good, *e.g.* on June 5. As a result, more image sets reach the threshold where image restoration becomes feasible, which significantly improves the temporal coverage during an observing campaign.

3.5. Speckle Masking Image Restoration

Obtaining sets of high-quality images is the goal of frame selection and input for *post-facto* image restoration. The standard method to restore HiFI images is the triple correlation or speckle masking technique (Lohmann, Weigelt, and Wirtitzer, 1983; Weigelt and Wirtitzer, 1983; de Boer, 1993; von der L uhe, 1993). The selected images are restored with the Kiepenheuer Institute Speckle Interferometry Package (KISIP, von der L uhe, 1993; W oger and von der L uhe, 2008; W oger, von der L uhe, and Rear-don, 2008). The algorithm includes an estimation of the long-exposure and speckle transfer functions and a field-dependent calibration of the Fourier amplitudes for the reconstructed sub-images (W oger and von der L uhe, 2007; W oger, 2010). The restored sub-images have a size of 256×256 pixels, which corresponds to $6.5'' \times 6.5''$ and is somewhat larger than the size of the isoplanatic patch under daytime seeing conditions (Rod-dier, Gilli, and Vernin, 1982; Irbah *et al.*, 1993). However, taking into account the apodization of the sub-images, their useful size reduces to about 200×200 pixels or about $5'' \times 5''$. Finally, the scattered light was corrected, which is introduced by Earth's atmosphere and imperfect telescope/instrument optics (see *e.g.* Bello Gonz alez and Kneer, 2008, and references therein), by deconvolution with an appropriate point-spread function.

The previous sections implicitly assumed that for HiFI observations $n_{\text{sel}} = 100$ and a 10-second time interval are appropriate choices for speckle masking image restoration. The underlying assumption for the latter parameter is that features are typically not moving faster than 2 km s^{-1} , which is already a concession based on the cost-benefit argument that only few pixels exhibit higher velocities. Studying transient events, thus requires different observing parameters. The optimal number of input images for image restoration depends on many factors, most notably on the image restoration algorithm and the seeing conditions. For example, multi-frame blind deconvolution (MFBD, L of-dahl, 2002; van Noort, Rouppe van der Voort, and L of-dahl, 2005) require just a few images of very good quality. To determine the proper number of input images, the best set in sequence No. 5 on June 5 was chosen for the analysis. Image quality metrics and photometric error were computed for $n_{\text{sel}} = 10, 20, \dots, 100, 200, \dots, 1600$ input images. The photometric error refers to the standard deviation of the intensity difference between restored image and the image restoration using all $n_{\text{set}} = 1600$

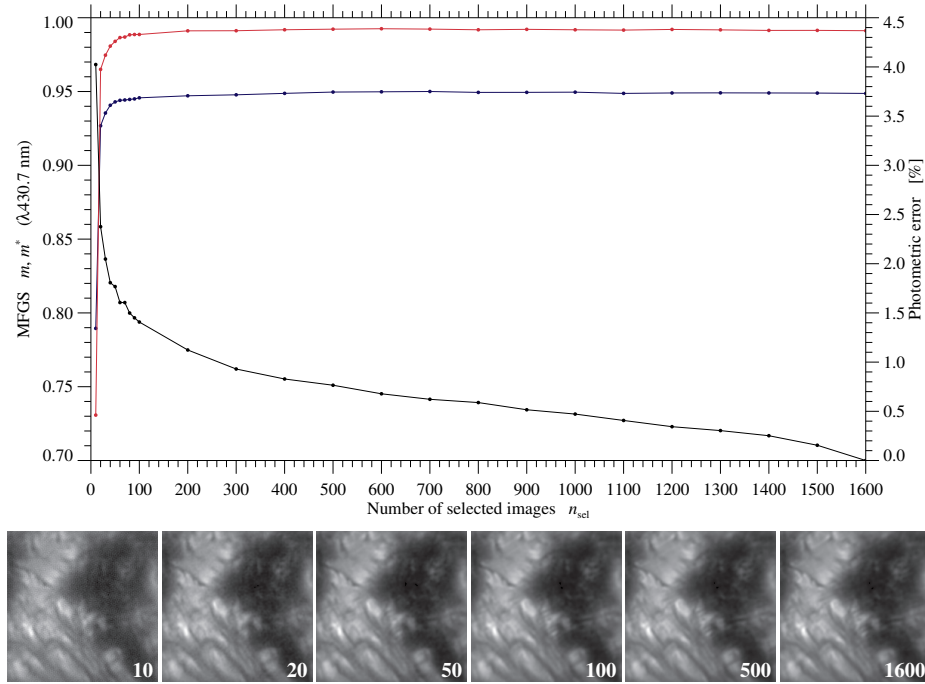


Figure 7. Image quality metrics MFGS m (red) and m^* (blue) as a function of the number of frame-selected input images n_{sel} that were used for the speckle masking image restoration. The sampling is ten times finer for $n_{\text{sel}} < 100$. The scale on the right side of the plot panel refers to the photometric error (black) using the restored image for $n_{\text{sel}} = 1600$ as a reference. The restored $5'' \times 5''$ -patches at the bottom provide a visual impression of the image quality as a function of n_{sel} , which is given in the lower-right corner of each patch.

images, divided by the mean intensity the restored reference image. This assumes that all images contribute to an improved image quality, which is valid as long as all images contain some diffraction-limited information. Obviously, if the seeing conditions are only mediocre, this assumption is violated, which might lead to a loss of image quality in the restored image. In the computation of image quality metrics and photometric error only the inner 4×4 restored isoplanatic patches were considered, after removal of the apodization borders.

The image quality metrics MFGS m and m^* are given in Figure 7 as a function of the number of input images n_{sel} . The behaviour of the metrics m^* and m' is very similar so that the latter was omitted to avoid clutter. The original MFGS implementation m is always larger than the locally computed m^* . Nonetheless, both metrics show the same trend, *i.e.* a steep increase for low values of n_{sel} , levelling out at $n_{\text{sel}} \approx 100$. The photometric error drops below 1% for $n_{\text{sel}} \approx 250$. Science cases based on high-resolution images typically require that morphological changes can be clearly identified, *i.e.* a good threshold for n_{sel} is reached when images are visually identical. The human eye can adapt to a wide range of intensities by brightness adaptation. However, discriminating between distinct gray levels at the same time is much more limited, and in this respect the dynamic range of the human eye is only 6–7 bits (Gonzalez and Woods, 2002). Therefore, $n_{\text{sel}} = 100$ is a good choice considering the marginal benefits. This is also

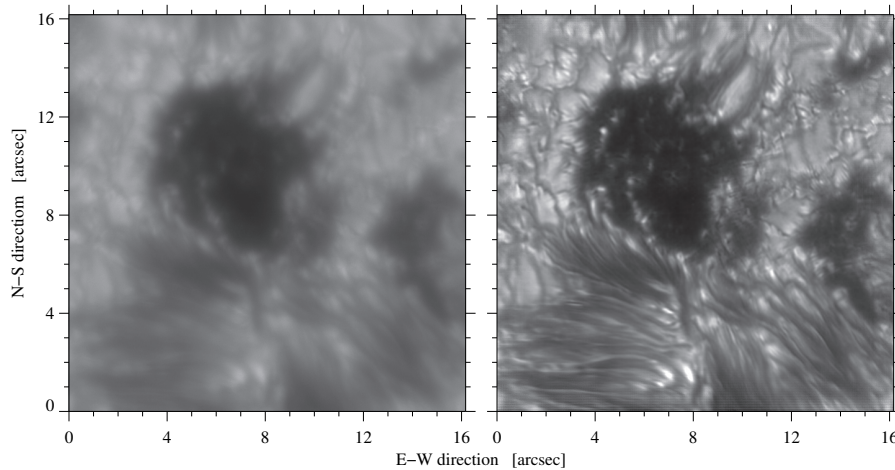


Figure 8. Best G-band image with $m = 0.84$ (left) and matching speckle-restored image with $m = 0.99$ (right) of a small sunspot with rudimentary penumbra in the trailing part of active region NOAA 12661 observed at 09:16:17 UT on 2017 June 5. Both images were scaled in the range $I/I_0 \in [0.1, 1.5]$, which is adapted to the intensity range of the restored G-band image.

illustrated in the bottom row of Figure 7, where restored isoplanatic patches are displayed as a function of n_{sel} . For $n_{\text{sel}} \leq 50$, noise still dominates the restored patches, including even “ringing” artifacts for $n_{\text{sel}} = 10$. This indicates that insufficient high-spatial frequency information was available in the Fourier domain. However, even for the case of just 10 input images, nearly diffraction-limited information is recovered, *i.e.* the phase recovery is already very good. On the other hand, photometric accuracy, which is mainly encoded in the Fourier amplitudes, scales roughly with the square root of the number of detected photons, *i.e.* the number of input images n_{sel} . This weak dependence results only in an improved photometry by a factor of four when increasing $n_{\text{sel}} = 100$ to 1600. The improvements are most clearly seen in bright-points superposed on a dark background, like umbral dots, where improved photometry removes much of the surrounding diffuse halo. An additional benefit of using more images in the restoration process is the better suppression of fixed-pattern noise. A more thorough analysis and discussion of photometric precision in speckle masking imaging is provided by Peck, Wöger, and Marino (2017) with an emphasis on AO-corrected images from large-aperture solar telescopes.

Figure 8 compares the best image of the best set in sequence No. 5 observed on June 5 with the corresponding speckle-restored and scattered-light corrected image, which shows a clear enhancement of the contrast and of the fine-structure contents. The horizontal fringing in the upper and lower parts of the restored G-band image is an artifact caused by the readout registers at the top and bottom of the sCMOS detectors, which create a fixed noise pattern with amplitudes and spatial frequencies close to those of solar fine structure. Consequently, these artifacts survive the image restoration and might even be enhanced in the process.

Purposefully, both images are scaled according to the intensity range of the restored G-band image to demonstrate that speckle masking image restoration affects both amplitudes and phases in the Fourier domain. G-band bright-points and substructure of

umbral dots are clearly visible with fine structure close to the diffraction limit of the *GREGOR* solar telescope. In addition, some penumbral filaments exhibit the distinctive dark cores first reported by Scharmer *et al.* (2002), which are extremely thin with a width of $0.2''$ or even less. Interestingly, some penumbral filaments appear almost at right angles to each other and almost tangential to the umbral core, which is indicative of highly sheared and twisted magnetic field lines.

The two-dimensional power spectrum of the speckle-restored image was averaged in the azimuthal direction to yield a one-dimensional power spectrum, which facilitates estimating the spatial cut-off frequency. This frequency is $15\text{--}16\text{ arcsec}^{-1}$ and corresponds to a structure size of $0.065''$. The exact value depends on the definition of the cut-off frequency and the settings of the noise filter. This value was also confirmed using MFBD for image restoration, where the cut-off frequency is slightly smaller, *i.e.* $14\text{--}15\text{ arcsec}^{-1}$, which corresponds to $0.069''$. The diffraction limit for the G-band images is $\lambda/D = 0.062''$, where λ is the observed wavelength, and D refers to the diameter of the telescope aperture. Thus, the spatial resolution of the restored image is close to the telescope's diffraction limit. In addition, the one dimensional power spectrum was essentially the same for speckle-restored images based on $n_{\text{sel}} = 100$ and 1600 input images. The G-band image depicted in the right panel of Figure 8 serves as an example of the imaging capabilities of the *GREGOR* solar telescope in the blue wavelength regime under very good but not excellent seeing conditions. Restored images of higher quality were observed with *GREGOR*'s high-resolution imagers but with lower image acquisition rate so that they could not be used for this study. Many examples of high-resolution images were presented in Schlichenmaier *et al.* (2016).

3.6. Field Dependency of Image Quality Metrics

As mentioned in Section 3.1, changing the order of summation and computing the similarity measure first yields an average MFGS value m^* on a pixel-by-pixel basis. The corresponding average ($n_{\text{seq}} = 40\,514$ and $53\,015$) two-dimensional MFGS maps are depicted in Figure 9 for G-band image sequences No. 5 observed on both June 4 and 5. Even though individual maps computed in this fashion are very noisy, the average maps strongly resemble the gradient magnitude of the average G-band images. Using the Scharr operator to calculate the gradient magnitude yields linear correlation coefficients $\rho = 0.67$ and 0.90 for the two MFGS maps in Figure 9. The correlation is higher, when the seeing is better. These findings reveal the inherent influence of the gradient magnitude operator, which is applied to both the original image and the median-filtered image. The superior performance of MFGS as an image quality metric, in contrast to simple gradient magnitude operators, results from the similarity measure casting the MFGS values into the interval $(0, 1]$. However, the MFGS maps in Figure 9 also clearly demonstrate the field dependency of the MFGS image quality metric, which has to be considered when comparing images of different scenes on the Sun.

Another way of assessing the field dependency is to compute the image quality parameters c_{rms} , m^* , m' , and m for sub-fields with the size of approximately the isoplanatic patch (160×160 pixels or $4'' \times 4''$). The results for image sequence No. 5 on June 4 are compiled in Figure 10 for 7×7 partially overlapping sub-fields. Higher values occur at the location of the central pores, which was also used for locking the AO systems. Systematic offsets between the upper and lower parts of the maps are caused by the presence

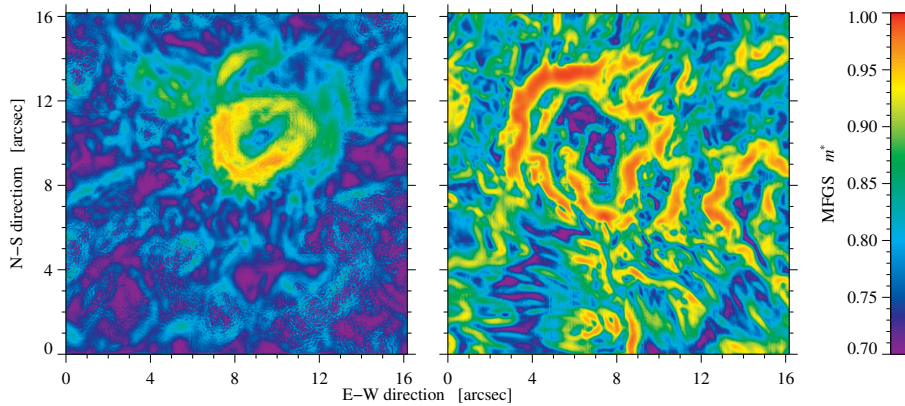


Figure 9. Two-dimensional maps of the average local MFGS values m^* for G-band image sequences No. 5 on 2017 June 4 (*left*) and June 5 (*right*), respectively.

of several small-scale pores in the upper part of the images. The low-resolution MFGS maps also agree with the high-resolution MFGS map in the left panel of Figure 9. In general, all maps exhibit a close resemblance and mainly differ in the absolute values. Unfortunately, these data are insufficient to determine the precise contributions to the field dependency either due to AO correction or due to the presence of contrast-rich structures. The June 5 data (not shown), with a more dispersed appearance caused by the dominant penumbral filaments, argue for a stronger contribution of the contrast-rich features. To isolate the AO contribution, locking on granulation will likely answer this question. However, such *GREGOR* data were not available. In many respects, the current results follow the trend already observed for other seeing parameters, *e.g.* the Fried-parameter r_0 and the differential image motion (*e.g.* Denker *et al.*, 2005, 2007b; Berkefeld *et al.*, 2010).

4. Discussion

The current (2560×2160 pixels) and next ($4k \times 4k$ pixels) generation of sCMOS cameras offer an image acquisition rate of 50 Hz in full-frame, global-shutter mode. This frame rate marks the point, where the MFGS curve $q(f_{\text{acq}})$ becomes flatter and eventually reaches a constant value (Figure 6), when f_{acq} approaches the coherence time of the prevailing daytime seeing conditions. Considering the diminishing marginal benefits of $q(f_{\text{acq}})$ for image restoration on the order of 30%, faster camera systems are desirable but come at a significant cost for data storage and processing. A possible solution are cameras with on-chip image buffers and fast image-caching so that external triggering becomes possible, either with ultra-fast, small-format cameras or with signals directly from the AO system. Ultimately, the latency between exposure time (typically 1–2 ms) and image acquisition time (now typically about 5–20 ms) has to be minimized as much as possible.

This latency can also be interpreted as the duty cycle of photon capture, which is only 16% for a image acquisition rate of 160 Hz and an exposure time of 1 ms. In

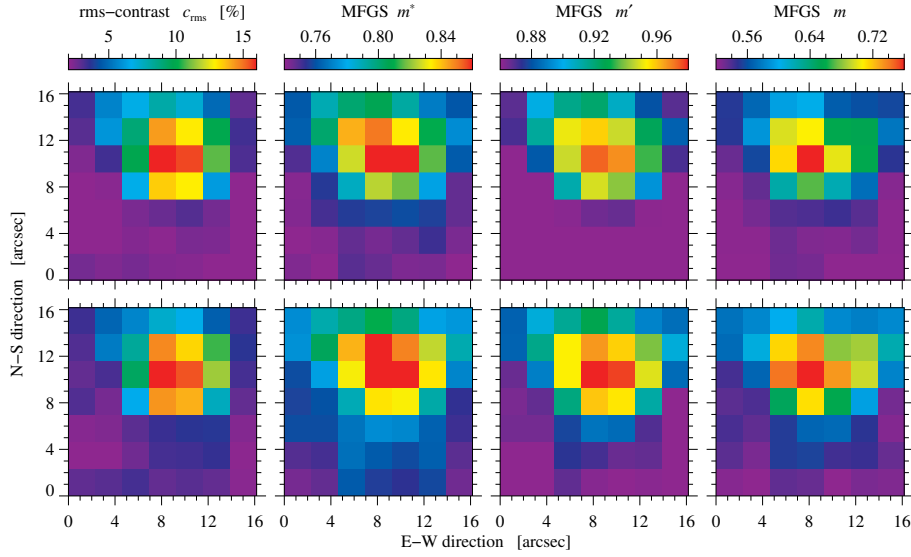


Figure 10. Field dependency of the average image quality respectively seeing parameters c_{rms} , m^* , m' , and m (left-to-right) for the blue continuum (top) and G-band (bottom) images computed for image sequence No. 5 on 2017 June 4. The tiles have a size of $4'' \times 4''$ and overlap by half. Thus, there is a positional mismatch if compared to G-band images.

principle, the exposure time can still be somewhat increased without affecting the image acquisition rate. However, the shorter exposure times ensured that they fell below the coherence time of the seeing. The above mentioned image acquisition rate of 50 Hz has also implications for imaging spectroscopy and spectropolarimetry. Taking the *GRECOR Fabry-Pérot Interferometer* (GFPI, Denker *et al.*, 2010; Puschmann *et al.*, 2012) as an example, typical image acquisition rates and exposure times are 10–15 Hz and 10–20 ms, respectively, with a duty cycle of only 15–20%. In this case, using cameras with a low read-out noise, a small full-well capacity (a few 10 000 e^-), a duty cycle close to 100%, and an image acquisition rate of at least 50 Hz will lead to significant performance gains – in particular, considering the “photon-starved” observations because of very narrow bandpasses (down to 2.5 pm).

Currently, both HiFi sCMOS cameras are attached to one control computer, where the images are saved to a RAID-0 array of eight SSDs at about 660 MB s^{-1} . Data are already written while new images are captured in a ring buffer. In the standard HiFi observing mode, two times $n_{\text{set}} = 500$ images are acquired in $\Delta t_{\text{set}} = 10$ s and recorded to disk in less than $\Delta t_{\text{rec}} = 20$ s, which includes overhead for real-time display of the blue continuum and G-band images and deferred writing from the ring buffer of the last images in the set. Already on site, all images undergo basic calibration and the best $n_{\text{set}} = 100$ images are selected and saved for *post-facto* image restoration. Thus, the results of this study are directly applicable to standard HiFi observations. However, the cadence of the restored images is two times slower than in principle possible with a data acquisition rate of $f_{\text{acq}} = 50$ Hz. However, in a master-slave configuration, where one sCMOS camera is attached to a dedicated computer, adequate data rates for several

cameras can be achieved, while the synchronization is provided by the PTU of the master computer.

The image restoration was carried out on a dedicated server at AIP containing four CPU sockets with 16 cores each, utilizing AMD Opteron 6378 processors with a clock speed of 2.4 GHz. Restoring a single isoplanatic patch takes about 90 s on a single core using 100 input images. Some overhead for reading and preparing the input images for parallel processing takes about the same amount of time. Adding more input images to the restoration process only raises the computing time linearly for the isoplanatic patches while the overhead essentially remains the same. Thus, frame selection also minimizes the computational resources. If sufficient cores are available, as for example on other, larger AIP computation clusters, processing in almost real-time (Denker, Yang, and Wang, 2001) becomes possible even for full-format 5-megapixel image sets. Pushing high-resolution imaging to the limit leads to instrument designs such as the *Visible Broadband Imager* (VBI, McBride *et al.*, 2012) for the 4-meter aperture *Daniel K. Inouye Solar Telescope* (DKIST, Tritschler *et al.*, 2016). Details of the VBI image acquisition and processing pipeline are laid out in Beard, Cowan, and Ferayorni (2014) incorporating AO-corrected and frame-selected images for real-time speckle restoration using on-site GPU technology.

Frame selection necessarily leads to unevenly sampled restored image sequences. The standard deviation of the effective observing time is about 2.4 s for a 10-second time interval, which indicates significant clustering of the moments with the best seeing conditions. However, on average the cadence of the restored image sequences remains unaffected. In most cases, it is sufficient to have context images with moderate cadence to follow major morphological changes or as input for optical flow techniques. In local correlation tracking (LCT, November and Simon, 1988; Verma and Denker, 2011), for example, a cadence of 60 s is sufficient, and an unevenly sampled time-series will have no impact when time-averaged flow maps are computed for studying persistent flow patterns – in particular, the effective observing time is known and thus the time interval that is needed to compute flow velocities for individual flow maps. For transient events and special purpose studies, such as the one at hand, all raw data, at the highest possible acquisition rate, can of course be kept.

The first high-cadence imaging systems for frame selection and image restoration became operational almost three decades ago (Scharmer, 1989). Video technology and fast frame grabbers already provided frame rates of 25–60 Hz at that time. Even though the dynamic range increased from 8-bit video images to 16-bit for current sCMOS detectors, noise still remains an issue. However, the fixed-pattern noise of sCMOS sensors rather than photon or read-out noise has to be treated carefully in subsequent image restoration. Nonetheless, the statement of Scharmer (1989) remains true that accurate photometry is not the goal of high-cadence imaging systems but nearly diffraction-limited imaging.

Deng *et al.* (2015) introduced MFGS to solar imaging and presented several short (200 frames) image sequences obtained in the TiO-band at $\lambda 705.8$ nm. The images were acquired at the 1-meter aperture *New Vacuum Solar Telescope* (Liu *et al.*, 2014) with a CMOS camera (2560×2160 pixels, image scale $0.04''$ pixel⁻¹) at a rate of 10–15 Hz and millisecond exposure times. The present study extends the original work by significantly increasing the statistics, introducing AO-corrected images, presenting strictly synchronous blue continuum and G-band images, raising the image acquisition

rate by a factor of ten, and proposing a different, local implementation of the MFGS image quality metric. The results do not support the conjecture by Deng *et al.* (2015) that the simple difference operator $G_x = [-1, 1]$ performs better than other implementations of gradient operators. There is a tendency that Sobel-type edge enhancement operators deliver higher MFGS values. However, scatter plots show a very tight correlation between different MFGS implementations, demonstrating a strictly monotonic though not necessarily a linear relationship. Directly comparing MFGS values from the original and current study proves to be difficult, considering different instrumental setups – in particular, the seeing conditions in the blue spectral region are more challenging compared to the near-infrared TiO-band. An alternative approach to evaluate image quality metrics is numerical modelling. Popowicz *et al.* (2017) used high-spatial resolution solar images from space taken with the Japanese *Hinode* mission (Kosugi *et al.*, 2007) and degraded them according to models of atmospheric turbulence. Thus, a large number of image quality metrics were quantitatively evaluated, with MFGS among the best performing methods.

The challenges, when high-cadence imaging meets large-format detectors, were already laid out for high-resolution imaging and imaging spectropolarimetry in Denker (2010). Based on first-hand experience with the *GREGOR* solar telescope, objective and robust image quality metrics are of utmost importance for navigating the large data volume from instruments such as GFPI and HiFI. In addition, the quality record provided by MFGS will not only facilitate searching databases, but at the same time, it will provide an extensive database of seeing conditions. Denker *et al.* (2018a) discussed data management and a collaborative research environment for the medium-sized *GREGOR* project. However, major research infrastructures such as DKIST and the future *European Solar Telescope* (EST, Collados *et al.*, 2010) require different approaches. The petascale cyberinfrastructure for the DKIST Data Center, for example, is summarized in Berukoff *et al.* (2016). Yet, image quality metrics like MFGS continue to provide valuable metadata for the expected data products.

5. Conclusions

The current study presents high-cadence and high-resolution observations of a representative sample of photospheric features including granulation, a compact pore, and a small sunspot with umbral dots and complex penumbral fine structure. The new sCMOS imaging system HiFI with two synchronized cameras allows us to record images in two different wavelengths simultaneously, which enabled us to obtain the wavelength and field dependency of image quality metrics and to assess the prevailing seeing conditions. An objective assessment becomes increasingly important, because the huge volume of imaging data generated by frame selection and lucky imaging necessitates an automatic inspection of image quality for image restoration and in database applications.

Pushing the limits of HiFI resulted in very high-cadence solar imaging at $f_{\text{acq}} = 160$ Hz with millisecond exposure times. Even in these image series, seeing is still variable on millisecond time-scales and shows variations from milliseconds to about one hour – the length of the observed time-series. Already in the standard full-frame mode, the data acquisition rate $f_{\text{acq}} = 50$ Hz of the sCMOS detectors outperforms the existing PCO.4000 facility cameras at *GREGOR* by a factor of ten. This is the minimum

data acquisition rate required to reap the benefits of frame selection, as demonstrated when quantifying the improvement in image quality $q(f_{\text{acq}})$ based on MFGS metrics in Section 3.4. Originally introduced by Deng *et al.* (2015), this method was applied in this study to AO-corrected blue continuum and G-band images, whereby establishing that frame selection significantly improves the temporal coverage of high-resolution observations, when the seeing becomes good enough for image restoration – in particular, when the seeing conditions are good to very good. The threshold $m = 0.65$ for G-band HiFI images is a good criterion for effective speckle masking image restoration.

The correlation analysis in Section 3.3 demonstrates that the three implementations of MFGS m , m' , and m^* behave very similar. The time-series of MFGS values are tightly correlated for G-band and blue continuum images. MFGS values for G-band images are systematically higher than for blue continuum images, which cannot be explained by the wavelength dependency of MFGS values, but is a consequence of the unique radiative transfer characteristics in this molecular band, which is also exploited in proxy-magnetometry of small-scale magnetic features. The original MFGS algorithm of Deng *et al.* (2015) has the shortest computation time but does not perform well, when the FOV contains features with a strong directional preference, whereas the other two MFGS implementations are very robust and deliver superior results for post-processing, when computational efficiency is not a major concern. The field dependency of MFGS was substantiated in Section 3.6, which complicates comparing time-series with different structural contents. However, within a time-series focusing on the same scene on the Sun, MFGS is a powerful tool to assess image quality and to identify the moments with the best seeing conditions. In comparison to all MFGS metrics, using the (granular) rms-contrast as a discriminator for image quality or seeing conditions yields unsatisfactory results.

In summary, the present work evaluated image quality metrics such as MFGS and image contrast for AO-corrected images. The present results support the notion that MFGS is an objective but likely not a universal image quality metric. For this reason, additional investigations are necessary studying scale dependency, center-to-limb variation, and susceptibility to noise and straylight, among others.

Acknowledgments The 1.5-meter *GREGOR* solar telescope was built by a German consortium under the leadership of the Kiepenheuer Institute for Solar Physics in Freiburg with the Leibniz Institute for Astrophysics Potsdam, the Institute for Astrophysics Göttingen, and the Max Planck Institute for Solar System Research in Göttingen as partners, and with contributions by the Instituto de Astrofísica de Canarias and the Astronomical Institute of the Academy of Sciences of the Czech Republic. We thank Drs. Peter Gömöry and Thomas Granzer for carefully reading the manuscript and providing valuable comments. CD, CK, HB, and MV were supported by grant DE 787/5-1 of the Deutsche Forschungsgemeinschaft (DFG). SJGM acknowledges support of project VEGA 2/0004/16 and is grateful for financial support from the Leibniz Graduate School for Quantitative Spectroscopy in Astrophysics, a joint project of the Leibniz Institute for Astrophysics Potsdam and the Institute of Physics and Astronomy of the University of Potsdam. This study is supported by the European Commission’s FP7 Capacities Program under the Grant Agreement number 312495.

Disclosure of Potential Conflicts of Interest The authors declare that they have no conflicts of interest.

References

- Acton, D.S., Smithson, R.C.: 1992, Solar Imaging with a Segmented Adaptive Mirror. *Appl. Opt.* **31**, 3161. DOI.
- Ballesteros, E., Collados, M., Bonet, J.A., Lorenzo, F., Viera, T., Reyes, M., Rodriguez Hidalgo, I.: 1996, Two-Dimensional, High Spatial Resolution, Solar Spectroscopy Using a Correlation Tracker. I. Correlation Tracker Description. *Astron. Astrophys. Suppl. Ser.* **115**, 353.
- Beard, A., Cowan, B., Ferayorni, A.: 2014, DKIST Visible Broadband Imager Data Processing Pipeline. In: Chiozzi, G., Radziwill, N.M. (eds.) *Software and Cyberinfrastructure for Astronomy III, Proc. SPIE* **9152**, 91521J. DOI.
- Bello González, N., Kneer, F.: 2008, Narrow-Band Full Stokes Polarimetry of Small Structures on the Sun with Speckle Methods. *Astron. Astrophys.* **480**, 265. DOI.
- Berkefeld, T., Soltau, D., Schmidt, D., von der Lühe, O.: 2010, Adaptive Optics Development at the German Solar Telescopes. *Appl. Opt.* **49**, G155. DOI.
- Berkefeld, T., Schmidt, D., Soltau, D., von der Lühe, O., Heidecke, F.: 2012, The GREGOR Adaptive Optics System. *Astron. Nachr.* **333**, 863. DOI.
- Berukoff, S., Hays, T., Reardon, K., Spiess, D., Watson, F., Wiant, S.: 2016, Petascale Cyberinfrastructure for Ground-Based Solar Physics: Approach of the DKIST Data Center. In: Chiozzi, G., Guzman, J.C. (eds.) *Software and Cyberinfrastructure for Astronomy IV, Proc. SPIE* **9913**, 99131F. DOI.
- Brandt, P.N., Wöhl, H.: 1982, Solar Site-Testing Campaign of JOSO on the Canary Islands in 1979. *Astron. Astrophys.* **109**, 77.
- Carlsson, M., Stein, R.F., Nordlund, Å., Scharmer, G.B.: 2004, Observational Manifestations of Solar Magnetoconvection: Center-to-Limb Variation. *Astrophys. J. Lett.* **610**, L137. DOI.
- Collados, M., Bettonvil, F., Cavaller, L., Ermolli, I., Gelly, B., Grivel-Gelly, C., Pérez, A., Socas-Navarro, H., Soltau, D., Volkmer, R.: 2010, European Solar Telescope: Project Status. In: Stepp, L.M., Gilmozzi, R., Hall, H.J. (eds.) *Ground-Based and Airborne Telescopes III, Proc. SPIE* **7733**, 77330H.
- de Boer, C.R.: 1993, Speckle-Interferometrie und ihre Anwendung auf die Sonnenbeobachtung. PhD thesis, Georg-August Universität Göttingen, Germany.
- Deng, H., Zhang, D., Wang, T., Ji, K., Wang, F., Liu, Z., Xiang, Y., Jin, Z., Cao, W.: 2015, Objective Image-Quality Assessment for High-Resolution Photospheric Images by Median Filter-Gradient Similarity. *Solar Phys.* **290**, 1479. DOI.
- Denker, C.: 2010, Instrument and Data Analysis Challenges for Imaging Spectropolarimetry. *Astron. Nachr.* **331**, 648. DOI.
- Denker, C., Yang, G., Wang, H.: 2001, Near Real-Time Image Reconstruction. *Solar Phys.* **202**, 63.
- Denker, C., Mascarinas, D., Xu, Y., Cao, W., Yang, G., Wang, H., Goode, P.R., Rimmele, T.R.: 2005, High-Spatial Resolution Imaging Combining High-Order Adaptive Optics, Frame Selection, and Speckle Masking Reconstruction. *Solar Phys.* **227**, 217. DOI.
- Denker, C., Tritschler, A., Rimmele, T.R., Richards, K., Hegwer, S.L., Wöger, F.: 2007a, Adaptive Optics at the Big Bear Solar Observatory: Instrument Description and First Observations. *Publ. Astron. Soc. Pac.* **119**, 170. DOI.
- Denker, C., Deng, N., Rimmele, T.R., Tritschler, A., Verdoni, A.: 2007b, Field-Dependent Adaptive Optics Correction Derived with the Spectral Ratio Technique. *Solar Phys.* **241**, 411. DOI.
- Denker, C., Balthasar, H., Hofmann, A., Bello González, N., Volkmer, R.: 2010, The GREGOR Fabry-Pérot Interferometer: A New Instrument for High-Resolution Solar Observations. In: McLean, I.S., Ramsay, S.K., Takami, H. (eds.) *Ground-Based and Airborne Instrumentation for Astronomy III, Proc. SPIE* **7735**, 77356M. DOI.
- Denker, C., von der Lühe, O., Feller, A., Arlt, K., Balthasar, H., Bauer, S.-M., Bello González, N., Berkefeld, T., Caligari, P., Collados, M., Fischer, A., Granzer, T., Hahn, T., Halbgewachs, C., Heidecke, F., Hofmann, A., Kentischer, T., Klvaňa, M., Kneer, F., Lagg, A., Nicklas, H., Popow, E., Puschmann, K.G., Rendtel, J., Schmidt, D., Schmidt, W., Sobotka, M., Solanki, S.K., Soltau, D., Staude, J., Strassmeier, K.G., Volkmer, R., Waldmann, T., Wiehr, E., Wittmann, A.D., Woche, M.: 2012, A Retrospective of the GREGOR Solar Telescope in Scientific Literature. *Astron. Nachr.* **333**, 810. DOI.
- Denker, C., Kuckein, C., Verma, M., González Manrique, S.J., Diercke, A., Enke, H., Klar, J., Balthasar, H., Louis, R.E., Dineva, E.: 2018a, Data Analysis and Management for High-Resolution Solar Physics – Image Restoration and Imaging Spectroscopy at the GREGOR Solar Telescope. *Astrophys. J. Suppl.* submitted.
- Denker, C., Kuckein, C., Verma, M., Balthasar, H., Diercke, A., Dineva, E., González Manrique, S.J., Louis, R.E., Seelemann, T., Hoch, S.: 2018b, High-Resolution Fast Imager (HiFI) for Image Restoration. *Astron. Nachr.* in preparation.
- Fried, D.L.: 1965, Statistics of a Geometric Representation of Wavefront Distortion. *J. Opt. Soc. Am. A* **55**, 1427. DOI.

- Fried, D.L., Mevers, G.E.: 1974, Evaluation of r_0 for Propagation Down through the Atmosphere. *Appl. Opt.* **13**, 2620. DOI.
- Gonzalez, R.C., Woods, R.E.: 2002, *Digital Image Processing*, Prentice-Hall, Upper Saddle River, New Jersey.
- Halbgewachs, C., Caligari, P., Glogowski, K., Heidecke, F., Knobloch, M., Mustedanagic, M., Volkmer, R., Waldmann, T.A.: 2012, The GREGOR Telescope Control System. *Astron. Nachr.* **333**, 840. DOI.
- Irbah, A., Borgnino, J., Laclare, F., Merlin, G.: 1993, Isoplanatism and High Spatial Resolution Solar Imaging. *Astron. Astrophys.* **276**, 663.
- Kitai, R., Funakoshi, Y., Ueno, S., Ichimoto, S.S.K.: 1997, Real-Time Frame Selector and its Application to Observations of the Horizontal Velocity Field in the Solar Photosphere. *Publ. Astron. Soc. Jpn.* **49**, 513. DOI.
- Kneer, F.: 2012, Hopes and expectations with GREGOR. *Astron. Nachr.* **333**, 790. DOI.
- Kosugi, T., Matsuzaki, K., Sakao, T., Shimizu, T., Sone, Y., Tachikawa, S., Hashimoto, T., Minesugi, K., Ohnishi, A., Yamada, T., Tsuneta, S., Hara, H., Ichimoto, K., Suematsu, Y., Shimojo, M., Watanabe, T., Shimada, S., Davis, J.M., Hill, L.D., Owens, J.K., Title, A.M., Culhane, J.L., Harra, L.K., Doschek, G.A., Golub, L.: 2007, The Hinode (Solar-B) Mission: An Overview. *Solar Phys.* **243**, 3. DOI.
- Kuckein, C., Denker, C., Verma, M., Balthasar, H., González Manrique, S.J., Louis, R.E., Diercke, A.: 2017, sTools – A Data Reduction Pipeline for the GREGOR Fabry-Pérot Interferometer and the High-Resolution Fast Imager at the GREGOR Solar Telescope. In: Vargas Domínguez, S., Kosovichev, A.G., Harra, L., Antolin, P. (eds.) *Fine Structure and Dynamics of the Solar Atmosphere*, IAU Symp. **327**, 20. DOI.
- Law, N.M., Mackay, C.D., Baldwin, J.E.: 2006, Lucky Imaging: High Angular Resolution Imaging in the Visible from the Ground. *Astron. Astrophys.* **446**, 739. DOI.
- Law, N.M., Mackay, C.D., Dekany, R.G., Ireland, M., Lloyd, J.P., Moore, A.M., Robertson, J.G., Tuthill, P., Woodruff, H.C.: 2009, Getting Lucky with Adaptive Optics: Fast Adaptive Optics Image Selection in the Visible with a Large Telescope. *Astrophys. J.* **692**, 924. DOI.
- Leenaarts, J., Rutten, R.J., Carlsson, M., Uitenbroek, H.: 2006, A Comparison of Solar Proxy-Magnetometry Diagnostics. *Astron. Astrophys.* **452**, L15. DOI.
- Liu, Z., Xu, J., Gu, B.-Z., Wang, S., You, J.-Q., Shen, L.-X., Lu, R.-W., Jin, Z.-Y., Chen, L.-F., Lou, K., Li, Z., Liu, G.-Q., Xu, Z., Rao, C.-H., Hu, Q.-Q., Li, R.-F., Fu, H.-W., Wang, F., Bao, M.-X., Wu, M.-C., Zhang, B.-R.: 2014, New Vacuum Solar Telescope and Observations with High Resolution. *Res. Astron. Astrophys.* **14**, 705. DOI.
- Löfdahl, M.G.: 2002, Multi-Frame Blind Deconvolution with Linear Equality Constraints. In: Bones, P.J., Fiddy, M.A., Millane, R.P. (eds.) *Image Reconstruction from Incomplete Data*, Proc. SPIE **4792**, 146. DOI.
- Lohmann, A.W., Weigelt, G., Wirmitzer, B.: 1983, Speckle Masking in Astronomy – Triple Correlation Theory and Applications. *Appl. Opt.* **22**, 4028. DOI.
- Lundstedt, H., Johannesson, A., Scharmer, G., Stenflo, J.O., Kusoffsky, U.: 1991, Magnetograph Observations with the Swedish Solar Telescope on La Palma. *Solar Phys.* **132**, 233. DOI.
- Mackay, C.: 2013, High-Efficiency Lucky Imaging. *Mon. Not. R. Astron. Soc.* **432**, 702. DOI.
- McBride, W.R., Wöger, F., Hegwer, S.L., Ferayorni, A., Gregory, B.S.: 2012, ATST Visible Broadband Imager. In: McLean, I.S., Ramsay, S.K., Takami, H. (eds.) *Ground-Based and Airborne Instrumentation for Astronomy IV*, Proc. SPIE **8446**, 84461B. DOI.
- November, L.J., Simon, G.W.: 1988, Precise Proper-Motion Measurement of Solar Granulation. *Astrophys. J.* **333**, 427. DOI.
- Peck, C.L., Wöger, F., Marino, J.: 2017, Influence of Speckle Image Reconstruction on Photometric Precision for Large Solar Telescopes. *Astron. Astrophys.* **607**, A83. DOI.
- Pesnell, W.D., Thompson, B.J., Chamberlin, P.C.: 2012, The Solar Dynamics Observatory (SDO). *Solar Phys.* **275**, 3. DOI.
- Popowicz, A., Radlak, K., Bernacki, K., Orlov, V.: 2017, Review of Image Quality Measures for Solar Imaging. *Solar Phys.* **292**, 187. DOI.
- Puschmann, K.G., Denker, C., Kneer, F., Al Erdogan, N., Balthasar, H., Bauer, S.M., Beck, C., Bello González, N., Collados, M., Hahn, T., Hirzberger, J., Hofmann, A., Louis, R.E., Nicklas, H., Okunev, O., Martínez Pillet, V., Popow, E., Seelemann, T., Volkmer, R., Wittmann, A.D., Woche, M.: 2012, The GREGOR Fabry-Pérot Interferometer. *Astron. Nachr.* **333**, 880. DOI.
- Qiu, P., Mao, Y.-N., Lu, X.-M., Xiang, E., Jiang, X.-J.: 2013, Evaluation of a Scientific CMOS Camera for Astronomical Observations. *Res. Astron. Astrophys.* **13**, 615. DOI.
- Rao, C.-H., Zhu, L., Rao, X.-J., Zhang, L.-Q., Bao, H., Ma, X.-A., Gu, N.-T., Guan, C.-L., Chen, D.-H., Wang, C., Lin, J., Jin, Z.-Y., Liu, Z.: 2016, First Generation Solar Adaptive Optics system for 1-m New Vacuum Solar Telescope at Fuxian Solar Observatory. *Res. Astron. Astrophys.* **16**, 23. DOI.
- Rimmele, T.R.: 2000, Solar Adaptive Optics. In: Wizinowich, P.L. (ed.) *Adaptive Optical Systems Technology*, Proc. SPIE **4007**, 218. DOI.

- Rimmele, T.R., Richards, K., Hegwer, S.L., Ren, D., Fletcher, S., Gregory, S., Didkovsky, L.V., Denker, C., Marquette, W., Marino, J., Goode, P.R.: 2003, Solar Adaptive Optics: A Progress Report. In: Wizinowich, P.L., Bonaccini, D. (eds.) *Adaptive Optical System Technologies II, Proc. SPIE* **4839**, 635. DOI.
- Rimmele, T.R., Richards, K., Hegwer, S., Fletcher, S., Gregory, S., Moretto, G., Didkovsky, L.V., Denker, C., Dolgushin, A., Goode, P.R., Langlois, M., Marino, J., Marquette, W.: 2004, First Results from the NSO/NJIT Solar Adaptive Optics System. In: Fineschi, S., Gummin, M.A. (eds.) *Telescopes and Instrumentation for Solar Astrophysics, Proc. SPIE* **5171**, 179. DOI.
- Roddier, F., Gilli, J.M., Vernin, J.: 1982, On the Isoplanatic Patch Size in Stellar Speckle Interferometry. *J. Opt. (Paris)* **13**, 63. DOI.
- Scharmer, G., Löfdahl, M.: 1991, Swedish Solar Telescope – Short Summary of Instrumentation and Observation Techniques. *Adv. Space Res.* **11**, 129. DOI.
- Scharmer, G.B.: 1989, High Resolution Granulation Observations from La Palma: Techniques and First Results. In: Rutten, R.J., Severino, G. (eds.) *Solar and Stellar Granulation, NATO Adv. Sci. Inst. (ASI) Ser. C* **263**, 161.
- Scharmer, G.B., Gudiksen, B.V., Kiselman, D., Löfdahl, M.G., Rouppe van der Voort, L.H.M.: 2002, Dark Cores in Sunspot Penumbra Filaments. *Nature* **420**, 151. DOI.
- Scharmer, G.B., Dettori, P.M., Löfdahl, M.G., Shand, M.: 2003, Adaptive Optics System for the New Swedish Solar Telescope. In: Keil, S.L., Avakyan, S.V. (eds.) *Innovative Telescopes and Instrumentation for Solar Astrophysics, Proc. SPIE* **4853**, 370. DOI.
- Schar, H.: 2007, Optimal Filters for Extended Optical Flow. In: Jähne, B., Mester, R., Barth, B., Schar, H. (eds.) *Complex Motion Lecture Notes in Computer Sciences* **3417**, Springer, Berlin, 14. DOI.
- Scherer, P.H., Schou, J., Bush, R.L., Kosovichev, A.G., Bogart, R.S., Hoeksema, J.T., Liu, Y., Duvall, T.L., Zhao, J., Title, A.M., Schrijver, C.J., Tarbell, T.D., Tomczyk, S.: 2012, The Helioseismic and Magnetic Imager (HMI) Investigation for the Solar Dynamics Observatory (SDO). *Solar Phys.* **275**, 207. DOI.
- Schlichenmaier, R., von der Lühe, O., Hoch, S., Soltau, D., Berkefeld, T., Schmidt, D., Schmidt, W., Denker, C., Balthasar, H., Hofmann, A., Strassmeier, K.G., Staude, J., Feller, A., Lagg, A., Solanki, S.K., Collados, M., Sigwarth, M., Volkmer, R., Waldmann, T., Kneer, F., Nicklas, H., Sobotka, M.: 2016, Active Region Fine Structure Observed at 0.08'' Resolution. *Astron. Astrophys.* **596**, A7. DOI.
- Schmidt, W., Kentischer, T.: 1995, Optical System of an Advanced Solar Correlation Tracker. *Astron. Astrophys. Suppl. Ser.* **113**, 363.
- Schmidt, W., von der Lühe, O., Volkmer, R., Denker, C., Solanki, S.K., Balthasar, H., Bello Gonzalez, N., Berkefeld, T., Collados, M., Fischer, A., Halbgewachs, C., Heidecke, F., Hofmann, A., Kneer, F., Lagg, A., Nicklas, H., Popow, E., Puschmann, K.G., Schmidt, D., Sigwarth, M., Sobotka, M., Soltau, D., Staude, J., Strassmeier, K.G., Waldmann, T.A.: 2012, The 1.5 Meter Solar Telescope GREGOR. *Astron. Nachr.* **333**, 796. DOI.
- Schröter, E.H., Soltau, D., Wiehr, E.: 1985, The German Solar Telescopes at the Observatorio del Teide. *Vistas Astron.* **28**, 519. DOI.
- Soltau, D., Volkmer, R., von der Lühe, O., Berkefeld, T.: 2012, Optical Design of the New Solar Telescope GREGOR. *Astron. Nachr.* **333**, 847. DOI.
- Sprung, D., Sucher, E., Stein, K., von der Lühe, O., Berkefeld, T.: 2016, Characterization of Optical Turbulence at the GREGOR Solar Telescope: Temporal and Local Behavior and its Influence on the Solar Observations. In: Stein, K.U., Gonglewski, J.D. (eds.) *Optics in Atmospheric Propagation and Adaptive Systems XIX, Proc. SPIE* **10002**, 1000205. DOI.
- Steele, I.A., Jermak, H., Copperwheat, C.M., Smith, R.J., Poshyachinda, S., Soonthorntham, B.: 2016, Experiments with Synchronized sCMOS Cameras. In: Holland, A.D., Beletic, J. (eds.) *High Energy, Optical, and Infrared Detectors for Astronomy VII, Proc. SPIE* **9915**, 991522. DOI.
- Steiner, O., Hauschildt, P.H., Bruls, J.: 2001, Radiative Properties of Magnetic Elements. I. Why are G-band Bright Points Bright? *Astron. Astrophys.* **372**, L13. DOI.
- Tritschler, A., Rimmele, T.R., Berukoff, S., Casini, R., Kuhn, J.R., Lin, H., Rast, M.P., McMullin, J.P., Schmidt, W., Wöger, F., DKIST Team: 2016, Daniel K. Inouye Solar Telescope: High-Resolution Observing of the Dynamic Sun. *Astron. Nachr.* **337**, 1064. DOI.
- van Noort, M., Rouppe van der Voort, L., Löfdahl, M.G.: 2005, Solar Image Restoration by Use of Multi-frame Blind Deconvolution with Multiple Objects and Phase Diversity. *Solar Phys.* **228**, 191. DOI.
- Verma, M., Denker, C.: 2011, Horizontal Flow Fields Observed in Hinode G-Band Images. I. Methods. *Astron. Astrophys.* **529**, A153. DOI.
- Volkmer, R., von der Lühe, O., Denker, C., Solanki, S., Balthasar, H., Berkefeld, T., Caligari, P., Collados, M., Fischer, A., Halbgewachs, C., Heidecke, F., Hofmann, A., Klvaňa, M., Kneer, F., Lagg, A., Popow, E., Schmidt, D., Schmidt, W., Sobotka, M., Soltau, D., Strassmeier, K.G.: 2010, GREGOR Solar Telescope. *Astron. Nachr.* **331**, 624.
- von der Lühe, O.: 1993, Speckle Imaging of Solar Small Scale Structure. I. Methods. *Astron. Astrophys.* **268**, 374.

-
- von der Lühe, O.: 1998, High-Resolution Observations with the German Vacuum Tower Telescope on Tenerife. *New Astron. Rev.* **42**, 493. [DOI](#).
- von der Lühe, O., Widener, A.L., Rimmele, T., Spence, G., Dunn, R.B.: 1989, Solar Feature Correlation Tracker for Ground-Based Telescopes. *Astron. Astrophys.* **224**, 351.
- von der Lühe, O., Schmidt, W., Soltau, D., Berkefeld, T., Kneer, F., Staude, J.: 2001, GREGOR: A 1.5-Meter Telescope for Solar Research. *Astron. Nachr.* **322**, 353.
- von der Lühe, O., Soltau, D., Berkefeld, T., Schelenz, T.: 2003, KAOS: Adaptive Optics System for the Vacuum Tower Telescope at Teide Observatory. In: Keil, S.L., Avakyan, S.V. (eds.) *Innovative Telescopes and Instrumentation for Solar Astrophysics, Proc. SPIE* **4853**, 187.
- Wang, H., Denker, C., Spirock, T., Goode, P.R., Yang, S., Marquette, W., Varsik, J., Fear, R.J., Nenow, J., Dingley, D.D.: 1998, New Digital Magnetograph at Big Bear Solar Observatory. *Solar Phys.* **183**, 1.
- Wedemeyer-Böhm, S., Rouppe van der Voort, L.: 2009, On the Continuum Intensity Distribution of the Solar Photosphere. *Astron. Astrophys.* **503**, 225. [DOI](#).
- Weigelt, G., Wirmitzer, B.: 1983, Image Reconstruction by the Speckle-Masking Method. *Opt. Lett.* **8**, 389.
- Wilken, V., de Boer, C.R., Denker, C., Kneer, F.: 1997, Speckle Measurements of the Centre-to-Limb Variation of the Solar Granulation. *Astron. Astrophys.* **325**, 819.
- Wöger, F.: 2010, Optical Transfer Functions Derived from Solar Adaptive Optics System Data. *Appl. Opt.* **49**, 1818. [DOI](#).
- Wöger, F., von der Lühe, O.: 2007, Field Dependent Amplitude Calibration of Adaptive Optics Supported Solar Speckle Imaging. *Appl. Opt.* **46**, 8015. [DOI](#).
- Wöger, F., von der Lühe, O.: 2008, KISIP: A Software Package for Speckle Interferometry of Adaptive Optics Corrected Solar Data. In: Bridger, A., Radziwill, N.M. (eds.) *Advanced Software and Control for Astronomy II, Proc. SPIE* **7019**, 70191E. [DOI](#).
- Wöger, F., von der Lühe, O., Reardon, K.: 2008, Speckle Interferometry with Adaptive Optics Corrected Solar Data. *Astron. Astrophys.* **488**, 375. [DOI](#).
- Zirin, H., Mosher, J.M.: 1988, The Caltech Solar Site Survey, 1965–1967. *Solar Phys.* **115**, 183. [DOI](#).